A Microbial Induced Synthesis Of Hydroxyapatite With High UV Light Photocatalytic Activity For Tetracycline Degradation

Ting Zeng[1], Yujie Yan[1], Juan Shen[1*], Ke Chen[1], Mi Tang[1], Zhicheng Guo[2], Bisheng Tan[3], Bo Jin[1]

[1]Department of Materials Science and Engineering, Southwest University of Science and Technology, Sichuan Mianyang, China; [2]Department of Nanotechnology, Southwest University of Science and Technology, Mianyang, China; [3]Department of Materials Science and Engineering, Institute of Chemical Materials Chinese Academy of Engineering Physics, Mianyang, China

Research Article

*For Correspondence:

Juan Shen, Department of Materials Science and Engineering, Southwest University of Science and Technology, Sichuan Mianyang 621010, China

E-mail: sj-shenjuan@163.com

ABSTRACT

More and more new materials have been developed, but the research on the development and utilization of the single-phase materials has been neglected. Assembled from nano-particles, a high specific surface area and porous hydroxyapatite (BI-HA) has been synthesized by feasible bacterial induction. The surface structure and morphology of the nanocomposites were characterized by Brunauer–Emmett–Teller (BET) apparatus, X-Ray Diffraction (XRD), Transmission Electron Microscopy (TEM). The results suggest the obtained BI-HA powder with porous morphology, which were composed of nanoparticles with (100) crystal plane. The photoactivity of different HA samples was evaluated by the photocatalytic degradation of Tetracycline hydrochloride (TC). The HA with (100) crystal plane displayed an obviously enhanced photocatalytic activity (75.33–86.43% for 60 min). Combined with experiments and DFT calculations, for the BI-HA with (100) crystal plane, it displayed better photocatalytic performance for photodegradation of TC. This study provides a viewpoint to fabricate high-performance nonmetal photocatalyst for wastewater treatment.

INTRODUCTION

Tetracycline (TC) is often detected from groundwater, surface water and sewage treatment systems as a new source of water pollution. It has caused "pseudo-persistence" pollution to water bodies, leading to an increase in drug-resistant pathogenic microorganisms, which has aroused widespread concern [1-3]. In recent years, physical and chemical methods, biological treatment methods, and chemical treatment methods have been devoted into the removal of TC from wastewater [4,5]. Among them, photocatalysis technology, as an advanced oxidation technology, has the advantages of utilizing the potential advantages of sunlight and high processing efficiency, and is used for the treatment of refractory organic pollutants [6-8]. However, there are not many reports on the degradation of antibiotics by photocatalytic technology, so it is necessary to intensify efforts to explore the use of photocatalytic technology to treat antibiotic wastewater [9,10].

Hydroxyapatite (HA), which is the main inorganic component in bone and enamel, has the advantages of good biocompatibility, safety and non-toxicity, and is therefore widely used in biomedical materials [11-13], drug carriers [14,15] and catalysts [16,17]. At the same time, due to the simple preparation process and low cost of HA, it is also widely used in the fields of catalyst carrier and water body repair. However, the photocatalytic activity of HA is still much lower than expected because of its poor charge transport, slow redox reaction kinetics, and low carrier mobility. Therefore, the development of a modification strategy to improve the HA charge kinetics is essential for achieving high performance HA [18-22]. At present, several modification strategies have been shown to improve the photocatalytic efficiency of HA, including material design and preparation [18], cocatalyst deposition [19] and elemental doping [22-24]. Several groups have reported that synthetic HA has better degradation properties of organic dyes by controlling the preparation conditions of hydroxyapatite. Nathanael et al. prepared a TiO_2-HAP composite by high-speed centrifugal gravity mixing of hydroxyapatite and $Ti(OH)^4$ colloids [25]. Compared with hydroxyapatite or TiO_2 alone, the composite catalyst was under ultraviolet light. It has better degradation ability to methyl orange [26] used hydroxyapatite to degrade calcium and magnesium indicators under ultraviolet light, which can remove 92% of COD and improve the biodegradability of dye wastewater [26]. They believe that UV irradiation can change the electronic structure of PO_4^{3-} on the surface of hydroxyapatite, generate oxygen vacancies and active $\bullet O_2^-$, and then degrade dye molecules. Although the research on the degradation of pollutants using hydroxyapatite composite photocatalyst has made some progress, there are some disadvantages. For example, hydroxyapatite can only be used as a support, and only plays an auxiliary role in the photocatalytic process. The preparation process of HA composite catalyst is complicated and their structure is unstable. Generally, the prepared composite catalyst can only be used under ultraviolet irradiation. Although the introduction of precious metals can increase the visible light activity of composite materials, it also increases manufacturing costs. Based on the characteristics of hydroxyapatite with different surface activity, the development of highly active hydroxyapatite photocatalyst has certain theoretical significance and practical value.

Here, HA particles were first prepared by using a novel bacterial induction method. The crystal structure, morphological characteristics, and specific surface area of HA particles were studied, and the photo catalysis of the prepared HA particles on the degradation of Tetracycline (TC) under ultraviolet light was studied. This synthesis method is different from the conventional synthesis methods. Phosphatase can be released by Bacillus subtilis to

control apatite mineralization. A large number of fine-pored, high specific surface areas HA crystal materials are surprisingly obtained. HA itself has good photo catalytic activity, and it does not need to add other photosensitive materials to enhance its photo catalytic performance. In addition, the intrinsic relationship between crystal morphological characteristics and photo catalytic activity of HA was preliminarily discussed. This work provided a simple method for improving the photocatalytic activity of HA, and also deepened the understanding of the photocatalytic mechanism of phosphate photocatalysts.

MATERIALS AND METHODS

Materials

Disodium phenyl phosphate dihydrate ($C_6H_5PO_4Na_2 \cdot 2H_2O$) was obtained from Aladdin (Shanghai, China), $CaCl_2$, HCl, NaCl, and NaOH were purchased from Kelong Chemical Inc (Sichuan, China), and all were analytical grade. Yeast powder and peptone were purchased from Beijing Aoboxing Bio-Tech Co., Ltd (Beijing, China), and both were biological reagent. *Bacillus subtilis* was purchased from China General Microbiological Culture Collection Center. Deionized water was used in all experiments.

Methods

Synthesis of hydroxyapatite: HA was synthesized by following steps. The first step, Luria-Bertani (LB) liquid medium was prepared and conducted by high pressure steam sterilization. The second step, the activated *Bacillus subtilis* was inoculated into LB medium (V/V=10%), and cultured in air bath oscillator under 37°C for a certain time to obtain bacteria solution with different concentration. The last step, $CaCl_2$ and $C_6H_5PO_4Na_2$ (Ca/P=1.67) were dissolved completely in deionized water at room temperature, and the solution was conducted by sterilization. And the obtained solution was added into the above bacteria solution under a clean bench, and the mixture was cultured in air bath oscillator under 37°C for 12 h. The obtained products were washed with ethyl alcohol and deionized water, and freeze dried for 24 h.

Characterization: The crystal structures of products were determined through X-ray powder diffraction (XRD; DMAX1400; Rigaku; Japan) with Cu Kα radiation, 2θ=3–80°. The images of the particle morphology and of the products were obtained using a scanning electron microscope (SEM; TM-4000; Hitachi; Japan) and transmission electron micro-144 scopy (TEM; Zeiss Libra 200FE; Germany). Fourier transform infrared spectroscopy (FT-IR; Nicolet-6700; PerkinElmer; America) in transmittance mode was used within the range of $400–4000\ cm^{-1}$ to identify the functional groups. Nitrogen adsorption–desorption isotherms were measured with an automatic surface area and porosity analyzer (AUTOSORB-1-C, Quantachrome, America) at the temperature of liquid nitrogen. The pore size distributions were derived from the adsorption branches of the isotherms using BJH theory. The particle size distribution of the as-synthesized powder was analyzed by using a laser particle size analyzer (90 plus; Brookhaven Instruments Corporation; America). The values of pH at the point of zero charge (pH pzc) of HA were analyzed using Zeta Potential Analyzer Zeta potential (zetaPALS; Brookhaven; America).

Photocatalytic experiments: The TC degradation activity of the as-prepared HA samples was measured under 300 W mercury lamp. Typically, 13.0 mg catalyst was dispersed in 50 mL aqueous solution containing TC with an initial concentration of 10 mg L^{-1}. The mixed solution was placed in the reactor, and the magnetic stirring was

carried out for 30 min under the dark environment to reach equilibrium of adsorption and desorption. At given time intervals, 5 mL solution was taken out every 15 min and centrifuged (4000 rpm, 5 min) to remove the catalyst. The concentration of supernatant was then measured using the UV–vis spectrometer.

Computational details: All DFT calculations were performed by using the Vienna Ab initio Simulation Package (VASP). The Generalized Gradient Approximation (GGA) with Perdew-Burker-Ernzerhof (PBE) functional was applied to address the nonlocal exchange correlation energy. DFT method with the Ueff=5.0 eV was used in all calculations [27]. The kinetic cutoff energy of 600 eV was adopted, and the Brillouin zone integration was sampled with the 2 × 2 × 3 k-point mesh. Structure optimization was deemed as converged until the force of all atoms less than 0.03 eV/Å, and the criteria of energy convergence were set to 1×10^{-5} Ev.

RESULTS AND DISCUSSION

Material characterization

The mechanism of BI-HA synthesis is presented in Figure 1. The morphologies of the as-prepared samples were investigated by SEM and (HR) TEM techniques. Figure 1 shows the SEM images of the products. Figures 2a and 2b indicate that the morphology of the products was of nanoparticles when the Ca^{2+} concentrations were 0.01 and 0.03 mol L^{-1}. When the Ca^{2+} concentration was 0.05 mol L^{-1}, these sheets were combined into uniform porous shapes with a rough surface (Figure 2c). Meanwhile, the Ca^{2+} concentration was 0.10 mol L^{-1} (Figure 2d), the obtained BI-HA with porous morphology, which were composed of nanoparticles. The TEM and HRTEM images of nanoparticles in Figure 2d are displayed in Figures 2e and 2f. The morphology was sheet-like and consisted of nanoparticles. The lattice spacing of 0.27 nm agreed with the distance between two (300) planes of BI-HA (Figure 1 and Figures 2a-2d).

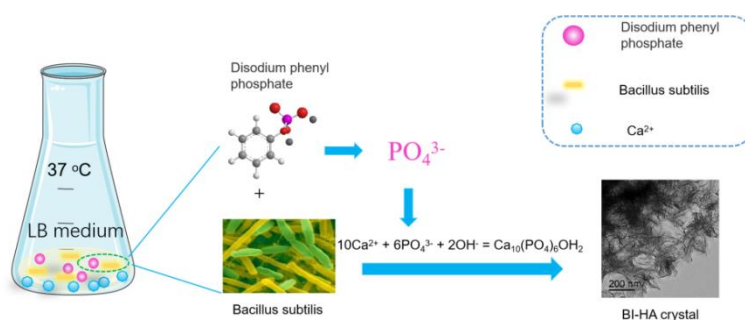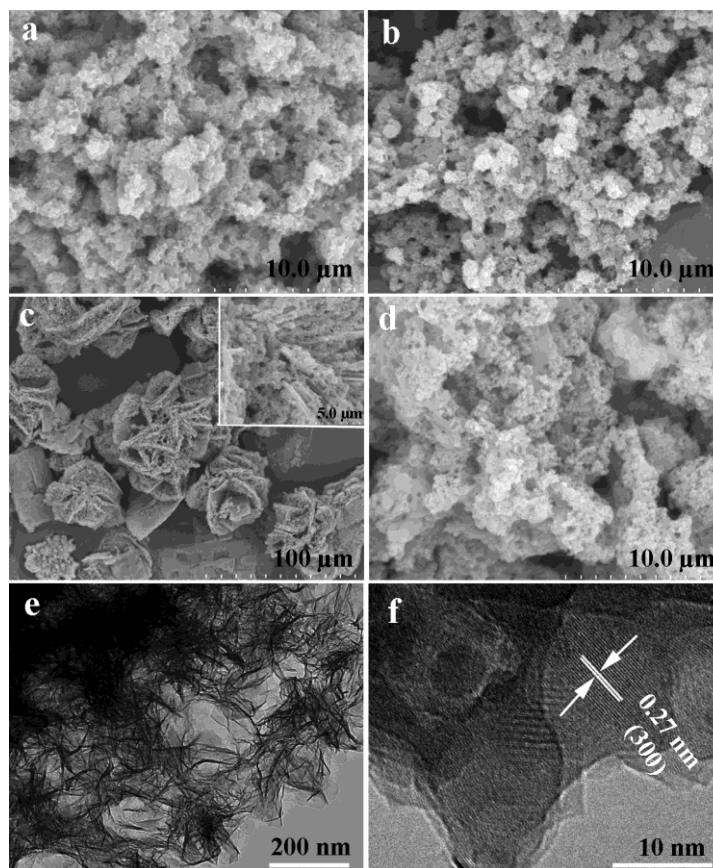**Figure 1**. Mechanism of synthesis of the BI-HA products induced by *Bacillus subtilis*.

Figure 2. SEM images of BI-HA prepared under different calcium ion concentrations: (a) 0.01 mol L^{-1}, (b) 0.03 mol L^{-1}, (c) 0.05 mol L^{-1}, and (d) 0.10 mol L^{-1}. TEM (e) and HRTEM (f) images of BI-HA prepared under calcium ion concentrations 0.10 mol L^{-1}.

The crystal structure of as-prepared catalysts was thoroughly investigated by X-Ray Diffraction (XRD). The XRD patterns of the products prepared under different Ca^{2+} concentrations are shown in Figure 3. The characteristic peaks in Figures 3a-3d remained consistent with the BI-HA according to the JCPDS card (NO. 09-0432), thereby indicating that the product was successfully converted into BI-HA. (Figures 3b and 3c) present the characteristic peaks of the standard card and the increase in intensity, thereby indicating that the high concentration of bacterial solution was conducive to BI-HA production. The phenomenon can be interpreted for the production of phosphatase during the metabolism of *B. subtilis* [28]. Disodium phenyl phosphate, as a substrate, slowly released PO_4^{3-} to the solution under the action of phosphatase. Then, the PO_4^{3-} and Ca^{2+} from the solution reacted to form porous BI-HA crystals under suitable conditions (Figure 3).

Figure 3. XRD patterns of BI-HA prepared under different calcium ion concentrations: (a) 0.01 mol L^{-1}, (b) 0.03 mol L^{-1}, (c) 0.05 mol L^{-1}, and (d) 0.10 mol L^{-1}.
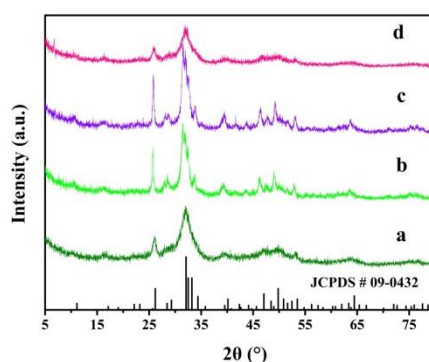
The FT-IR spectra of disodium phenyl phosphate dihydrate and the products prepared under different bacterial concentrations are presented in Figure 4. Figure 4a shows the FT-IR spectrum of $C_6H_5PO_4Na_2 \cdot 2H_2O$. The CH stretching modes for monosubstituted benzene were found in the region $3105-2900$ cm^{-1}. The bands at 1596, 1489 and 1238 cm^{-1} were assigned as benzene ring-stretching modes. The bands observed at 1159 and 1115 cm^{-1} were assigned to the asymmetric stretching vibrations. Bands at 1009 and 995 cm^{-1} were assigned to the PO_4 symmetric stretching vibrations. The bands at 886, 763 and 734 cm^{-1} were assigned as the out-of-plane CH deformations of the phenyl ring [29]. Compared with Figure 4a, the adsorption bands of Figures 4b-4e were not consistent with Figure 4a. The BI-HA characteristic peaks appeared in the FT-IR spectra shown in Figures 4b and 4e. The wide absorption bands at c, a. 3434 and 1633 cm^{-1} are attributed to the adsorbed water. The absorption peak at 1427 cm^{-1} may be caused by the carbon dioxide in the aqueous solution or air. The peaks at 1113 (v3), 1092 (v3), 963(v1), 602 (v4), and 564 cm^{-1} (v4) are the characteristic bands for PO_4^{3-}. This phenomenon demonstrated that the addition of *Bacillus subtilis* solution could favour the formation of BI-HA products (Figure 4).

Figure 4. FT-IR spectra of (a) disodium phenyl phosphate dihydrate and BI-HA prepared under different calcium ion concentrations: (a), (b) 0.01 mol L^{-1}, (c) 0.03 mol L^{-1}, (d) 0.05 mol L^{-1}, and (e) 0.10 mol L^{-1}.
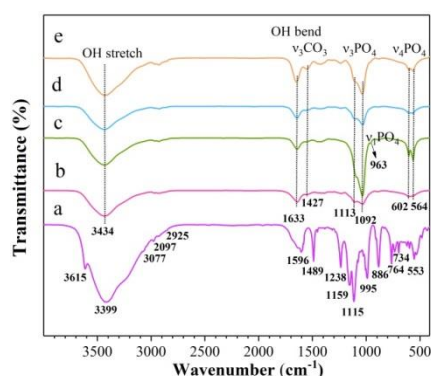
As presented in Figure 5, the nitrogen adsorption and desorption isotherms and the pore size distribution curves of the product were investigated. According to the IUPAC classification, all the isotherms in Figures 5a-5d were assigned to types IV and H3 hysteresis loops, thereby confirming the existence of mesopores. Figures 5a1-5d1 showed that the pore size distribution was irregular and comprised a mixture of mesopores and micropores. As the concentration of Ca^{2+} changed from 0.01 mol L^{-1} to 0.1 mol L^{-1}, the specific surface area of the product changed from 133.8 m^2 g^{-1}, 173.8 m^2 g^{-1}, 196.7 m^2 g^{-1}, to 73.61 m^2 g^{-1}. Meanwhile, the pore structure of the product mainly composed of mesopores according to the analysis of the total pore and mesoporous volumes (Figure 5).

Figure 5. Nitrogen adsorption, desorption isotherms and the corresponding BJH pore size distribution curves of BI-HA prepared under different calcium ion concentrations: (a, a1) 0.01 mol L^{-1}, (b, b1) 0.03 mol L^{-1}, (c, c1) 0.05 mol L^{-1}, and (d, d1) 0.10 mol L^{-1}.
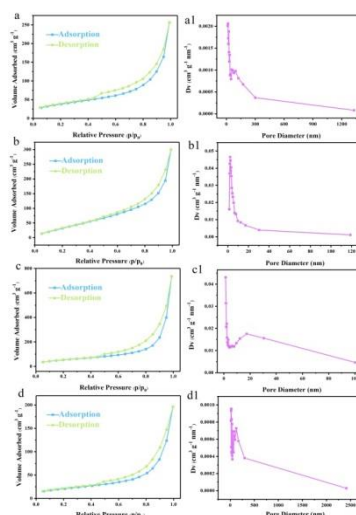
Photocatalytic degradation of TC

In order to evaluate the photocatalytic activity of different synthetic BI-HA powders, the degradation of TC using BI-HA1, BI-HA2, BI-HA3 and BI-HA4 were tested under UV light irradiation. Firstly, due to the larger specific surface area of the prepared hydroxyapatite samples, the C/C0 ratio under dark reaction conditions for 75 minutes was studied. As shown in Figure 6a, lower than 22% TC was adsorbed onto the as-prepared photocatalysts in the dark, indicating relatively poor adsorption capacity of TC over these samples. Under UV light irradiation, the blank experiment test revealed that the self-degraded of TC is nearly negligible shown in Figure 6b. The BI-HA photocatalysts displayed a good photocatalytic activity (74.4~86.4% for 60 min) for TC degradation. Among those samples, BI-HA4 showed the highest photocatalytic efference (86.4%) after 60 min (Figure 6).

Figure 6. Dark reaction (a) and photocatalytic degradation (b) of TC by as-prepared catalysts. Note: (—⬭—) B1-HA1; (—⬭—) B1-HA2; (—⬭—) B1-HA3; (—⬭—) B1-HA4; (⬤) Blank.
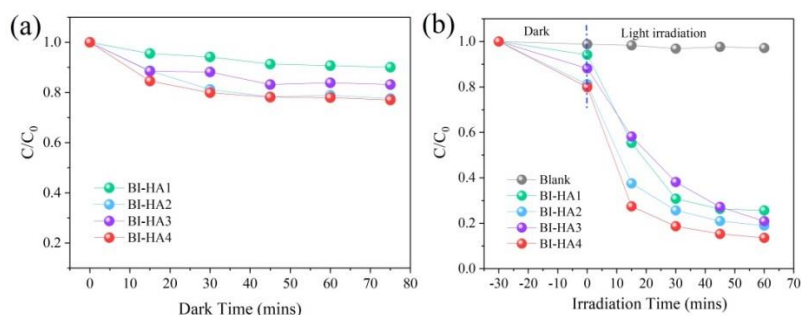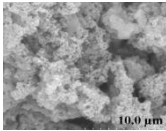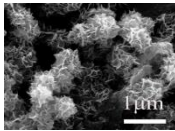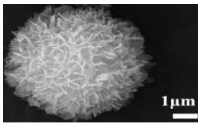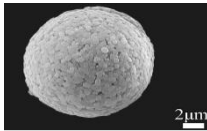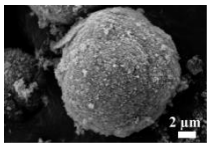

Possible photocatalytic mechanism

 The development of photocatalytic materials has thus been an important requirement. Various types of materials ranging from natural inorganic materials to organic polymers have received a remarkable interest for degradating TC from solution [30,31]. This research is different from previous synthetic ideas. A novel synthetic method to

simulate the microbial biomineralization in nature is used, and hydroxyapatite crystals with a large specific surface area were obtained (Table 1). It consists of nanoscale ultrafine particles and their dense aggregates (Figure 2). The BI-HA samples exhibited enhanced photocatalytic performance by photocatalytic degradation of TC under UV light irradiation. Structures always show great influence on the absorption of solar energy and transfer of photogenerated electron-hole paries. HRTEM result showed the synthetic BI-HA nanoparticle with the platelet crystal growth direction was (100). For the comparison of the photocatalytic degradation effects of TC with (100) or (001) crystal plane HA samples, we selected different HA samples for TC photodegradation experiments (Table 1). As shown in Figure 7, HA photocatalysts with different crystallite structures and morphologies displayed different photocatalytic activity. The HA with (100) crystal plane displayed an obviously enhanced photocatalytic activity (75.33–86.43% for 60 min), while the HA with (001) crystal plane exhibited poor photocatalytic degradation effiency (18.0 % for 60 min) for TC degradation. It shows that as-prepared BI-HA4 has a high degradation capacity, thereby indicating that BI-HA4 with a (100) crystal plane, a specific morphology and specific surface is of great significance in photocatalytic activity (Table 1) (Figure 7).

Table 1. Comparison of different morphologies and specific surface area hydroxyapatite photocatalytic values.

| HA synthetic method	Specific surface area (m² g⁻¹)	Crystal growth crystal face	Photocatalytic value (%)	Morphology	Synthetic method Ref.
Bacterial - Induced method (BI-HA)	73.61	(100)	86.43		Current work
Double Interfacial Diffusion method (DID-HA)	188.5	(100)	75.33		Xia et al. 2019
Hydrothermal method (Hy-HA1)	130.8	(100)	80.14		Qi et al. 2016
Hydrothermal method (Hy-HA2)	_	(001)	54.77		Qi et al. 2015
Hard Template method (HT-HA1)	Ball-shaped 201.3	(001)	55.72		Xia et al. 2018
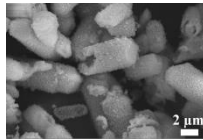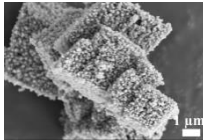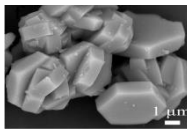
Hard Template method (HT-HA2)	Rod-shaped 190.9	(001)	47.20		Xia et al. 2018
Hard Template method (HT-HA3)	Block-shaped 106.3	(001)	51.70		Xia et al. 2018
Double Surfactants method (DS-HA)	–	(001)	20.76		Chen et al. 2020

Figure 7. Photocatalytic degradation of TC by as-prepared different HA catalysts with different crystallite structures and morphologies. Note: (⬤) Control; (━⬤━) DS-HA; (━⬤━) HT-HA3; (━⬤━) HT-HA2; (━⬤━) HT-HA1; (━⬤━) Hy-HA2 ; (━⬤━) Hy-HA1; (━⬤━) DID-HA; (━⬤━) B1-HA4.
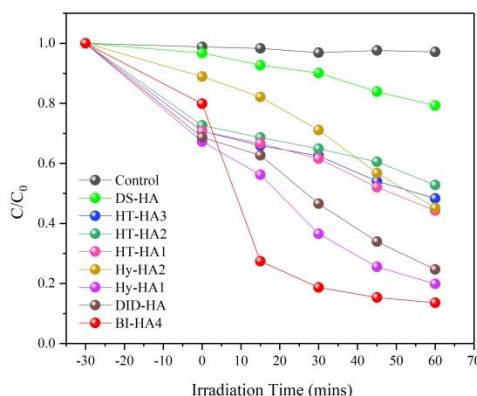
Under the action of HA, UV light excites the H_2O or O_2 molecules in the surrounding air to produce $\bullet OH^-$ and $\bullet O_2^{-}$. After UV excitation, the electrons are transferred to O_2 to form $\bullet O_2^-$, while $\bullet OH^-$ may be due to the reaction of $\bullet O_2^-$ and H_2O. These free radicals can effectively decompose Tetracycline, etc., to generate CO_2, H_2O and other hydrocarbon compounds.

Under the catalysis of HA, tetracycline will react as follows:

$HA + h\nu \rightarrow HA\bullet$

$HA\bullet + O_2 \rightarrow HA + \bullet O_2^-$

$O_2^- + H_2O \rightarrow \bullet OH^-$

$OH^- + \bullet O_2^- + TC \rightarrow$ degradation products (CO_2, C_nH_n, etc.)
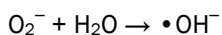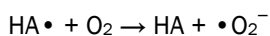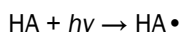
We know that the photoinduced electron/hole depends largely on the energy band structure and electronic Density of State (DOS) of photocatalyst [32,33]. As shown in Figures 8a and 8b, the Valence Band (VB) of HA is mainly contributed by the O-2p orbit below Fermi level, while the Conduction Band (CB) is attributed to the Ca-4s orbit above Fermi level. However, due to the derivative discontinuity of the exchange correlation function, the bandgap (E_g) is underestimated by using DFT calculation [34-42]. The existence of HA (100) effectively reduces the band gap. Compared with HA (001) in Figure 8a, the VB width of HA (100) is increased. Therefore, the separation of photoinduced electrons in HA (100) will be enhanced, which indicates a better photocatalytic oxidation ability (Figure 8).

Figure 8. Total Density of States (DOS) and Projected Density of States (PDOS) of (a) HA (001) and (b) HA (100). The dotted lines at energy zero represent the fermi level.
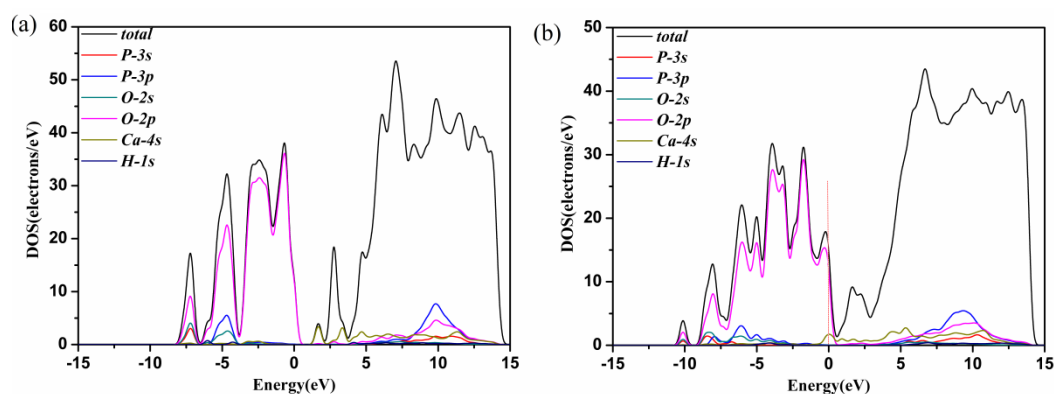
CONCLUSION

The HA photocatalysts had been obtained through a Bacillus subtilis induction method with special flower-like structure were obtained. The obtained BI-HA with porous morphology self-assembled by sheets, which were composed of nanoparticles, had an average particle size of 0.66 μm and a high specific surface area. For the BI-HA with (100) crystal plane, it displayed better photocatalytic performance for photodegradation of TC. High reactive sites on the HA made it an effective photocatalyst for degradation of TC (above 86%). The BI-HA powder with (100) crystal plane shows dramatic photocatalytic activity, confirming their practical use in water purification.

ACKNOWLEDGEMENTS

REFERENCES

1. Zhou Y, et al. Transformation of tetracycline antibiotics during water treatment with unactivated peroxymonosulfate. Chem Eng J, 2020;379: 122-378.

2. Islam GM, et al. The effect of tetracycline on the structure of the bacterial community in a wastewater treatment system and its effects on nitrogen removal. J Hazard Mater. 2019;371:130-137.

3. Du B, et al. Impacts of long-term exposure to tetracycline and sulfamethoxazole on the sludge granules in an anoxic-aerobic wastewater treatment system. Sci Total Environ. 2019;684:67-77.

4. Qu Z, et al. Recycling of groundwater treatment sludge to prepare nano-rod erdite particles for tetracycline adsorption. J Clean Prod. 2020;257:120-462.

5. Zhao J, et al. Application of humic acid changes the microbial communities and inhibits the expression of tetracycline resistance genes in 4-chlorophenol wastewater treatment. J Environ Manage. 2019;250:109-463.

6. Khodadadi M, et al. The catalytic activity of FeNi3@SiO2 magnetic nanoparticles for the degradation of tetracycline in the heterogeneous Fenton-like treatment method. J Water Process Eng, 2019;32:100-943.

7. Zhang Y, et al. Rapid degradation of tetracycline hydrochloride by heterogeneous photocatalysis coupling persulfate oxidation with MIL-53(Fe) under visible light irradiation. J Hazard Mater. 2020;392: 122-315.

8. Wang X, et al. Combination of photocatalysis with hydrodynamic cavitation for degradation of tetracycline. Chem Eng J, 2017;315: 274-282.

9. Yu J, et al. Quantification of the local magnetized nanotube domains accelerating the photocatalytic removal of the emerging pollutant tetracycline. Appl Catal B Environ. 2019;248:450-458.

10. Wei X, et al. Synthesis of tetragonal prismatic γ-In2Se3 nanostructures with predominantly {110} facets and photocatalytic degradation of tetracycline. Appl Catal Environ .2020:260:118-218.

11. Yadav S, et al. Synthesis, characterization, mechanical and biological properties of biocomposite based on zirconia containing 1393 bioactive glass with hydroxyapatite. Ceram Int. 2020;46: 10442-10451.

12. Ferraris S, et al. Bioactive materials: In vitro investigation of different mechanisms of hydroxyapatite precipitation. Acta Biomaterialia. 2020;102:468-480.

13. He F, et al. Hydroxyapatite mineral enhances malignant potential in a tissue-engineered model of ductal carcinoma in situ (DCIS). Biomaterials, 2019;224:119-125.

14. Yi Z, et al. Hierarchical porous hydroxyapatite fibers with a hollow structure as drug delivery carriers. Ceram Int. 2016;42: 19079-19085.

15. Xiong H, et al. Mitochondria and nuclei dual-targeted heterogeneous hydroxyapatite nanoparticles for enhancing therapeutic efficacy of doxorubicin. Biomaterials. 2016;94: 70-83.

16. Schiavoni M, et al. Focus on the catalytic performances of Cu-functionalized hydroxyapatites in NH3-SCR reaction. Appl Catal A: Gen. 2018;563:43-53.

17. Shariffuddin JH, et al. Greener photocatalysts: Hydroxyapatite derived from waste mussel shells for the photocatalytic degradation of a model azo dye wastewater. Chem Eng Res Des. 2013;91:1693-1704.

18. Reeta Mary I, et al. Surfactant-free solvothermal synthesis of Hydroxyapatite nested bundles for the effective photodegradation of cationic dyes. J Phys Chem Solids. 2018;116:180-186.

19. Valizadeh S, et al. Modified Fe3O4- hydroxyapatite nanocomposites as heterogeneous catalysts in three UV, Vis and Fenton like degradation systems. Appl Surf Sci, 2014; 319:358-366.

20. Ekka B, et al. Synthesis of hydroxyapatite-zirconia nanocomposite through sonochemical route: A potential catalyst for degradation of phenolic compounds. J Environ Chem Eng. 2018; 6:6504-6515.

21. Lv C, et al. Hydroxyapatite supported Co3O4 catalyst for enhanced degradation of organic contaminants in aqueous solution: Synergistic visible-light photo-catalysis and sulfate radical oxidation process. Microchem J. 2019;149: 103-159.

22. Jiraborvornpongsa N, et al. Effects of MoOx modification on photocatalytic activity of hydroxyapatite and Ti-doped hydroxyapatite. Adv Powder Technol. 2019; 30:1617-1624.

23. Huang J, et al. Developing titania-hydroxyapatite-reduced graphene oxide nanocomposite coatings by liquid flame spray deposition for photocatalytic applications. J Eur Ceram Soc. 2017;37:3705-3711.

24. Ishisone K, et al. Experimental and theoretical investigation of WOx modification effects on the photocatalytic activity of titanium-substituted hydroxyapatite. Appl Catal B Environ. 2020;264:118-126.

25. Joseph Nathanael A, et al. Mechanical and photocatalytic properties of hydroxyapatite/titania nanocomposites prepared by combined high gravity and hydrothermal process. Compos Sci Technol. 2010;70: 419-426.

26. Reddy MP,et al. Hydroxyapatite photocatalytic degradation of calmagite (an azo dye) in aqueous suspension. Appl Catal B: Environ. 2007;69:164-170.

27. Yang Z, et al. Oxygen vacancy pairs on CeO2(110): A DFT+U study. Phys Lett A. 2009;373:2786-2792.

28. Molla MAZ, et al. Microbial mineralization of organic phosphate in soil. Plant Soil. 1984;78:393-399.

29. Anto PL, et al. Vibrational spectroscopic studies and ab initio calculations of phenyl phosphate disodium salt. J Raman Spectrosc. 2010;41:113-119.

30. Lyu J, et al. Removal of tetracycline by BiOBr microspheres with oxygen vacancies: Combination of adsorption and photocatalysis. J Phys Chem Solids. 2019;129: 61-70.

31. Zhang Y, et al. Coupling of heterogeneous advanced oxidation processes and photocatalysis in efficient degradation of tetracycline hydrochloride by Fe-based MOFs: Synergistic effect and degradation pathway. Chem Eng J. 2019;369:745-75.

32. Xiong H, et al. Enhancing degradation and mineralization of tetracycline using intimately coupled photocatalysis and biodegradation (ICPB). Chem Eng J. 2017;316:7-14.

33. Zhang Y, Enhanced photocatalytic performance of Bi4Ti3O12 nanosheets synthesized by a self-catalyzed fast reaction process. Ceram Int. 2018;44:23014-23023.

34. Peng C, et al. Hybrids of Two-Dimensional Ti3C2 and TiO2 Exposing {001} Facets toward Enhanced Photocatalytic Activity. Acs Appl Mater Interfaces. 2016; 8:6051-6060.

35. Xia X, et al. A facile synthesis of hydroxyapatite for effective removal strontium ion. J Hazard Mater. 2019;368:326-335.

36. Qi YC, et al. Hierarchical porous hydroxyapatite microspheres: synthesis and application in water treatment. J Mater Sci. 2016;51:2598-2607.

37. Qi Y, et al. The morphology control of hydroxyapatite microsphere at high pH values by hydrothermal method. Adv Powder Technol. 2015;26:1041-1046.

38. Xia X, et al. Synthesis of hollow structural hydroxyapatite with different morphologies using calcium carbonate as hard template. Adv Powder Technol. 2018;29:1562-1570.

39. Chen R, et al. The synthesis of hydroxyapatite crystals with various morphologies via the solvothermal method using double surfactants. Mater Lett. 2020;259:126-134.

40. Zhang YC, et al. Role of oxygen vacancies in photocatalytic water oxidation on ceria oxide: Experiment and DFT studies. Appl Catal B: Environ. 2018; 224:101-108.

41. Lu J, et al. Periodic density functional theory study of ethylene hydrogenation over Co3O4 (111) surface: The critical role of oxygen vacancies. Appl Surf Sci. 2016;371: 61-66.

42. Pan L, et al. Undoped ZnO abundant with metal vacancies. Nano Energy. 2014;9:71-79.